Available online at www.sciencedirect.com
ScienceDirect
Journal of Computational Physics 224 (2007) 970–991
JOURNAL OF COMPUTATIONAL PHYSICS
www.elsevier.com/locate/jcp

Multi-domain hybrid spectral-WENO methods for hyperbolic conservation laws

Bruno Costa [a], Wai Sun Don [b,*]

[a] Departamento de Matemática Aplicada, IM-UFRJ, Caixa Postal 68530, Rio de Janeiro, RJ, C.E.P. 21945-970, Brazil
[b] Division of Applied Mathematics, Brown University, Providence, RI 02912, United States

Received 23 February 2006; received in revised form 12 October 2006; accepted 1 November 2006
Available online 19 December 2006

Abstract

In this paper, we introduce the multi-domain hybrid Spectral-WENO method aimed at the discontinuous solutions of hyperbolic conservation laws. The main idea is to conjugate the non-oscillatory properties of the high order weighted essentially non-oscillatory (WENO) finite difference schemes with the high computational efficiency and accuracy of spectral methods. Built in a multi-domain framework, subdomain adaptivity in space and time is used in order to maintain the solutions parts exhibiting high gradients and discontinuities always inside WENO subdomains, while the smooth parts of the solution are kept in spectral ones. A high order multi-resolution algorithm by Ami Harten is used to determine the smoothness of the solution in each subdomain. Numerical experiments with the simulation of compressible flow in the presence of shock waves are performed.
© 2006 Elsevier Inc. All rights reserved.

Keywords: Spectral; WENO; Multi-resolution; Multi-Domain; Hybrid; Conservation laws

1. Introduction

The fine scale and delicate structures of physical phenomena related to turbulence demand the utilization of high order methods when performing numerical simulations. Spectral methods are non-dispersive and non-dissipative and, therefore, well fitted to this task when the solutions involved are smooth. However, in the modeling of compressible turbulent flows by means of the inviscid Euler equations, the development of finite time discontinuities generates global O(1) oscillations, known as the Gibbs phenomenon, that causes loss of accuracy and numerical instability. Filtering of small scales has been used to stabilize the spectral scheme in shock calculations [15], however the Gibbs oscillations still remain in the solution.

In Fig. 1, the density of the Lax shock tube problem with Riemann initial conditions was obtained with a Chebyshev collocation method stabilized with a 16th-order exponential filter. Note that the oscillations also occur at a smaller scale on the edges of the rarefaction wave due to the discontinuities at the derivative of the

* Corresponding author. Tel.: +1 401 863 2250.
E-mail addresses: bcosta@ufrj.br (B. Costa), wsdon@cfm.brown.edu (W.S. Don).

0021-9991/$ - see front matter © 2006 Elsevier Inc. All rights reserved.
doi:10.1016/j.jcp.2006.11.002

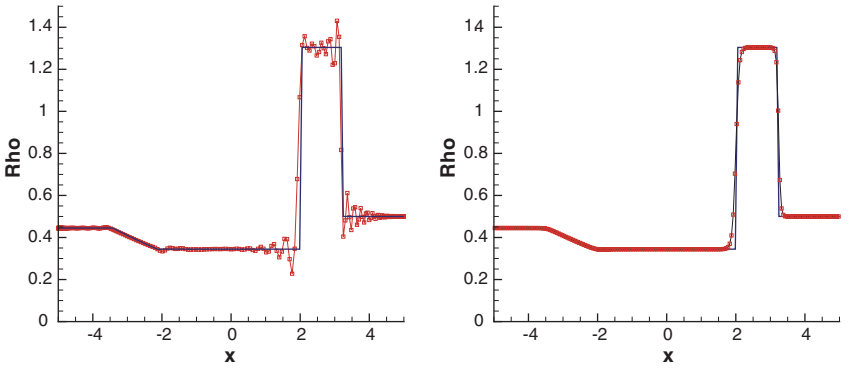

Fig. 1. The density of the Lax problem as computed by (left) the Chebyshev collocation solution with the Gibbs oscillations and (right) the fifth-order characteristic-wise WENO finite difference scheme. The exact solution is represented by the solid line.

density. The use of heavier filtering is not recommended as it would remove the fine scale physical structures which are important for the overall fidelity of the simulation.

Reconstruction techniques such as the direct and inverse Gegenbauer expansions (see [5,30] and references contained therein) have achieved some success as a postprocessing treatment to remove the Gibbs oscillations. These techniques followed the achievement of relevant theoretical results demonstrating convergence properties of spectral approximations of discontinuous solutions. For instance, Gottlieb and Tadmor [6] proved that, for linear problems, the moments of the numerical solution computed by spectral methods are spectrally accurate. Lax [10] had argued that high order information about the solution is contained in high resolution schemes, even for nonlinear problems. Hence highly accurate essentially non-oscillatory solution can be extracted from the seemingly oscillatory noisy data. Tadmor [12] showed convergence of spectral methods for nonlinear scalar equations. Nevertheless, the rapid growth rate of the Gegenbauer polynomials cause several numerical problems which are difficult to overcome. Very often, the domain must be subdivided in order to apply the Gegenbauer reconstruction when dealing with complex and localized flow structures.

These numerical difficulties associated with the global spectral method are among the main reasons why local nonlinear adaptive shock capturing finite differences have been the method of choice when dealing with nonlinear conservation laws. Among these, the most commonly used are the essentially non-oscillatory schemes (ENO) [23]. In order to avoid numerical oscillations, ENO schemes bias the local stencil, discarding interpolations across discontinuities when computing the tendencies of the numerical solution. The weighted essentially non-oscillatory (WENO) method [25] is an improvement over the ENO method with the introduction of a convex combination of all the available stencils. WENO achieves optimal order of accuracy at smooth parts of the solution with the same stencil size of ENO. Nevertheless, the intrinsic numerical dissipation of WENO schemes, although necessary to properly capture shock waves, damps relevant small scales, even when these are smooth components of the solution. Fig. 1 also shows a solution of the same Lax problem obtained with a fifth-order characteristic-wise WENO finite difference scheme. Note the smearing of the shock, the contact interface and of the edges of the rarefaction wave. The numerical dissipation can be reduced by increasing the number of points, as well as the order of the WENO scheme which, however, would make the scheme expensive to apply. This would also means waste of computational effort since it would not change the situation of well resolved structures at the smooth regions of the solution. Moreover, the fixed order of the finite differences does not provide the exponential resolution of spectral schemes.

This paper aims at the conjugation of the spectral and WENO methods when solving hyperbolic equations with discontinuous solutions. The general idea is to build a multi-domain scheme, forming a global adaptive mesh composed of WENO and spectral subdomains in a way that discontinuities of the solution are always contained within WENO subdomains and the smooth components remain in spectral ones. A smoothness measurement device triggers the switching of the subdomains from spectral to WENO and reciprocally, according to the local behavior of the solution. For instance, the algorithm takes care of moving discontinuities by changing the spectral subdomains in their way to WENO ones and switching WENO subdomains in

their trails to spectral subdomains, guaranteeing higher numerical efficiency than the classical single-domain WENO method and non-oscillatory solutions when compared to the classical single-domain spectral method. Moreover, the application of spectral methods at smooth regions avoids the heavy machinery employed by the characteristic-wise WENO finite difference algorithm such as the evaluation of the Jacobian of the fluxes, the global Lax–Friedrichs flux splitting and the forward and backward characteristics projections.

The multi-domain hybrid Spectral-WENO method (Hybrid) here proposed can also be thought of as an improvement to the classical spectral method by using the "WENO technique" to approximate discontinuities, in the same way that physical filtering is used. Based on the multi-domain framework, the Gibbs phenomenon is effectively avoided, since there will be no spectral approximation of discontinuities, which also discards the need of any postprocessing technique.

This paper is organized as follows: approximation theory of spectral methods is briefly discussed in Section 2. In Section 3, WENO finite differences schemes are described and Harten's multi-resolution algorithm is presented in Section 4. The Hybrid method along with its interfaces treatment and subdomain switching procedure are introduced in Section 5. In Section 6, we apply the Hybrid method to the standard shock-tube problems with Riemann initial data, to the Shock-Entropy wave interaction and the Blastwave problems. Conclusions are given in Section 7.

2. Spectral methods

We start this section with a quick description of Galerkin and collocation spectral methods which, in their simplest forms, make use of a global smooth basis $\{\phi_k(x),\ k = 0,\ldots,N\}$ to represent the numerical solution. After that, we discuss the Gibbs phenomenon for piecewise smooth functions and the utilization of filtering to stabilize the spectral discretization of hyperbolic conservation laws.

2.1. Spectral collocation methods

In the Galerkin approach, a generic function $f(x)$ is projected into the set of basis function $\phi_k(x)$ as

$$P_N f(x) = \sum_{k=0}^{N} a_k \phi_k(x), \tag{1}$$

where P_N is the projection operator. The coefficients a_k are

$$a_k = \int f(x)\phi_k(x)w(x)\,\mathrm{d}x, \tag{2}$$

with the appropriate weight function $w(x)$ that depends on the nature of the physical solution:

- For periodic problems, the natural basis functions are the trigonometric polynomials of degree k, $\phi_k(x) = \mathrm{e}^{\mathrm{i}\pi kx}$ with weight function $w(x) = 1$ and $x \in [-1, 1)$.
- For non-periodic problems in a finite domain $x \in [-1, 1]$, Chebyshev polynomials $\phi_k(x) = T_k(x)$ with $w(x) = (1 - x^2)^{\frac{1}{2}}$ or, Legendre polynomials $\phi_k(x) = L_k(x)$ with $w(x) = 1$ are the most used bases.

The collocation version of spectral methods approximates a function $f(x)$ by an interpolating polynomial given by

$$I_N f(x) = \sum_{k=0}^{N} a_k \phi_k(x), \quad a_k = \sum_{i=0}^{N} \omega_i f(x_i)\phi_k(x_i), \tag{3}$$

where I_N is the interpolation operator, x_i and ω_i are the Gauss–Lobatto quadrature nodes and weights respectively (Gauss–Radau and Gauss nodes can also be used). Alternatively,

$$I_N f(x) = \sum_{j=0}^{N} f(x_j) g_j(x), \tag{4}$$

where $g_j(x)$ are the cardinal functions: Lagrangian interpolation polynomials of degree N such that $g_j(x_i) = \delta_{ij}$. For the Lagrangian interpolation polynomials based on the Chebyshev Gauss–Lobatto points $x_i = \cos(\pi i/N)$, $i = 0, \ldots, N$, the cardinal functions are given by

$$g_j(x) = \frac{(-1)^{j+1}(1-x^2)T'_N(x)}{c_j N^2 (x - x_j)}, \tag{5}$$

where $c_0 = c_N = 2$, $c_j = 1$, $j = 1, \ldots, N-1$ and $T_N(x)$ is the Nth degree Chebyshev polynomial of the first kind. The derivatives of $f(x)$ at the collocation points x_i can be computed via Eqs. (3) or (4). The former makes use of the fast cosine transform (CFT) algorithm and the latter uses a matrix–vector algorithm. More details can be found in [2].

The derivative of the interpolating polynomial is simply given by the $(N-1)$th degree polynomial

$$(I_N f)'(x) = \sum_{j=0}^{N} f(x_j) g'_j(x), \tag{6}$$

providing an easy way to obtain the approximated values $(I_N f)'(x_i)$: we only need to multiply the vector composed of the function values $\{f(x_j)\}_{j=0}^{N}$ by the differentiation matrix D, whose elements $D_{ij} = g'_j(x_i)$, in closed form is given

$$\begin{aligned} D_{kj} &= \frac{c_k}{c_j}\frac{(-1)^{j+k}}{x_k - x_j}, \quad k \neq j, \\ D_{kk} &= -\frac{1}{2}\frac{x_k}{1-x_k^2}, \quad k \neq 0, N, \\ D_{00} &= -D_{NN} = \frac{2N^2+1}{6}. \end{aligned} \tag{7}$$

In this way, numerical differentiation through collocation spectral methods can be accomplished through matrix–vector multiplication. For the small N used in this study, the roundoff error using the form above did not pose a significant problem.

2.2. Conservation laws: Gibbs phenomenon and filtering

The approximation error in spectral methods depends only on the regularity of the approximated function. A typical error estimate is of the form

$$|f(x) - P_N f(x)| \leqslant C N^{\frac{1}{2}-p} \left(\int_0^{2\pi} |f^{(p)}(\xi)|^2 \, \mathrm{d}\xi \right)^{\frac{1}{2}}, \tag{8}$$

where C is a constant independent of N and $f^{(p)}$ denotes the pth derivative of f. We see that the approximation error decays as $O(N^{-p})$ for any C^p function and if the function is analytic then

$$|f(x) - P_N f(x)| \leqslant C \mathrm{e}^{-\alpha N}, \tag{9}$$

for some $\alpha > 0$, resulting in exponential convergence. Similar results hold for the pseudospectral (collocation) formulation. However, in the case of piecewise smooth functions, the order of accuracy is reduced to O(1) due to the well known Gibbs phenomenon.

Fig. 2 shows the Fourier collocation approximations to a sawtooth function with a discontinuity at $x = 0$. Note that the overshoot and undershoot oscillations do not decrease with the increasing number of grid points N.

Other important properties of spectral methods are their inherent non-dissipativity and non-dispersiveness, which are good properties when important conservation principles need to be respected at the numerical level. This lack of dissipation, however, becomes an issue when dealing with discontinuous solutions of conservation laws, in particular, when spectral methods are applied to nonlinear hyperbolic equations in the conservation form and the problem of an entropy satisfying solution arises. In fact, there is no artificial dissipation in spectral methods to indicate that their solutions are limits of a dissipative process. This problem had been

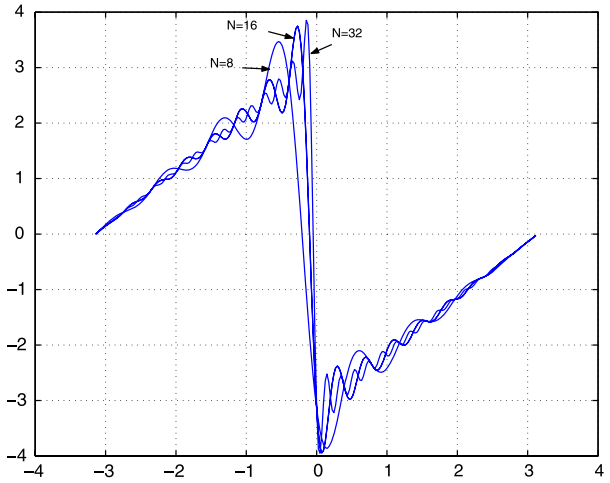

Fig. 2. Gibbs phenomenon in the spectral approximation of a sawtooth function.

addressed in [13] and in the references contained therein, where it has been shown that with a suitable addition of a spectrally small dissipation to the high modes, the method is stable and entropic solutions are obtained.

The utilization of a low pass filtering in spectral methods helps both to mitigate the Gibbs phenomenon and to introduce the necessary artificial dissipation for hyperbolic problems. Considering the Fourier approximation (The process is analogous for the Chebyshev case):

$$f_N(x) = \sum_{k=-N}^{N} a_k e^{i\pi kx}, \quad x \in [-1, 1), \tag{10}$$

filtering is introduced by means of the modified sum

$$f_N^{\sigma}(x) = \sum_{k=-N}^{N} \sigma\left(\frac{k}{N}\right) a_k e^{i\pi kx}, \tag{11}$$

where, following Vandeven [14], $\sigma(\omega)$ is a pth order, $p > 1$, $C^p[-1,1]$, filter function satisfying

$$\begin{aligned} &\sigma(0) = 1, \qquad \sigma(\pm 1) = 0, \\ &\sigma^{(j)}(0) = 0, \quad \sigma^{(j)}(\pm 1) = 0, \quad j \leqslant p, \end{aligned} \tag{12}$$

where $\sigma^{(j)}$ denotes its jth derivative.

It has been shown in [14] that the filtered sum (11) approximates a discontinuous function in smooth regions with exponential accuracy.

In this work, we make use of the exponential filter function

$$\sigma(\omega) = \exp(-\alpha|\omega|^{\beta}), \tag{13}$$

where $-1 \leqslant \omega = k/N \leqslant 1$, $|k| = 0, \ldots, N$, β is the order of the filter and $\alpha = -\ln \epsilon$, where ϵ is the machine zero. In Fig. 3 the solution of the periodical inviscid Burgers equation is obtained with a Fourier collocation method stabilized with a 16th-order Exponential filter.

It is worth saying that no amount of filtering other than a heavy one ($p \leqslant 2$), can remove the Gibbs oscillations from the solution. The use of such a filter, however, also incurs in removal of small and median scale structures rendering the solution unusable and inaccurate.

In practice, when solving differential equations one uses a high order Exponential filter at every time step to maintain stability and a post-processing technique [5,28,30] at the end of the calculation to recover a non-oscillatory solution from the oscillatory one. These post-processing techniques, however, are not practical, particularly, for multi-dimensional problems. As it is evident from Fig. 3, in order to recover the full accuracy

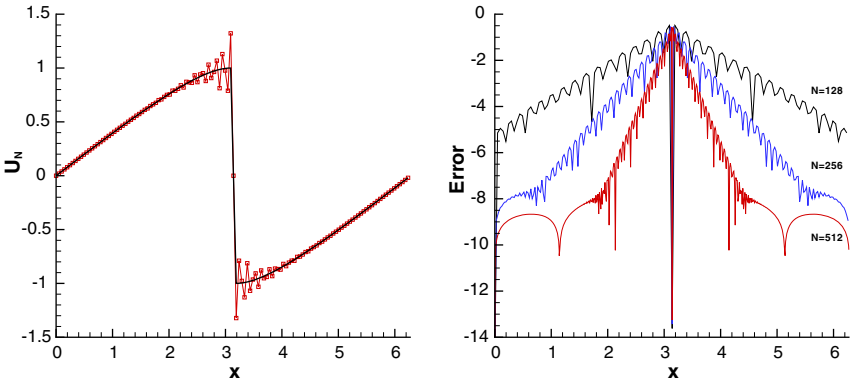

Fig. 3. (Left) Exact and Fourier spectral solution of the Burgers equation with a 16th-order exponential filter and $N = 128$ collocation points. (Right) Convergence of the solution with $N = 128,256,512$. The error is in the log10 scale.

in any region where the function is continuous, one has to use a different idea. In the next section we introduce non-oscillatory finite differences schemes as the next step to build this new idea in the form of a hybrid scheme.

3. Weighted essentially non-oscillatory schemes

In this section, we describe essentially non-oscillatory conservative finite difference schemes to be applied at systems of conservation laws described by the general equation:

$$u_t + f(u)_x = 0. \tag{14}$$

We will first present a general high order conservative central scheme approximation to (14). After that, we will describe the adaptive stencil choosing process of ENO and WENO schemes that leads to their non-oscillatory properties.

3.1. Conservative schemes

Being conservative is an important property of a numerical approximation due to the Lax–Wendroff theorem which states that numerical solutions of conservative schemes, whenever they converge, converge to weak solutions of the conservation law [10]. A conservative finite-difference formulation for hyperbolic conservation laws requires high-order consistent numerical fluxes at the cell boundaries in order to form the flux difference across the uniformly-spaced cells.

Consider an uniform grid defined by the points $x_i = i\Delta x$, $i = 0,\ldots,N$, which are also called cell centers, with cell boundaries given by $x_{i+\frac{1}{2}} = x_i \pm \frac{\Delta x}{2}$. Eq. (14) is semi-discretized in time by the method of lines, yielding the following system of ordinary differential equations

$$\frac{\mathrm{d}u_i(t)}{\mathrm{d}t} = -\left.\frac{\partial f}{\partial x}\right|_{x=x_i}, \quad i = 0,\ldots,N, \tag{15}$$

where $u_i(t)$ is a numerical approximation to the cell center value $u(x_i,t)$.

The conservative property of the spatial discretization is obtained by implicitly defining a numerical flux function $h(x)$ as

$$f(x) = \frac{1}{\Delta x}\int_{x-\frac{\Delta x}{2}}^{x+\frac{\Delta x}{2}} h(\xi)\,\mathrm{d}\xi, \tag{16}$$

such that the spatial derivative in (15) is exactly approximated by a conservative finite difference formula at the cell boundaries,

$$\frac{\mathrm{d}u_i(t)}{\mathrm{d}t} = \frac{1}{\Delta x}(h_{i+\frac{1}{2}} - h_{i-\frac{1}{2}}), \tag{17}$$

where $h_{i\pm\frac{1}{2}} = h(x \pm \frac{\Delta x}{2})$. High order polynomial interpolations to $h_{i\pm\frac{1}{2}}$ are computed using known grid values of f.

Note that the order of the polynomial interpolation of $h_{i\pm\frac{1}{2}}$ will set the order of the spatial approximation of the overall scheme (17). Due to the symmetry of the stencils used for the polynomial interpolations, the order of approximation of the right-hand side of (17) will be the same order of the polynomial approximation of $h(x)$, even after division by Δx, and not, as expected, one order less.

Let us now solve the problem of finding a kth order central polynomial approximation to $h_{i+\frac{1}{2}}$. Let

$$\hat{h}(x) = a_0 + a_1 x + \cdots + a_{k-1}x^{k-1}, \tag{18}$$

be a $(k-1)$th degree polynomial approximation to $h(x)$ and $\hat{f}(x)$ be the polynomial (also of degree $k-1$) obtained by integration of (16) after the substitution of $h(x)$ by $\hat{h}(x)$. The polynomial coefficients are found after evaluating $\hat{f}(x)$ at the grid points of any k nodes stencil around $x_{i+\frac{1}{2}}$. For instance, if $k = 3$, the coefficients a_0, a_1, a_2 can be obtained as functions of the grid point values f_{i-1}, f_i and f_{i+1}. Once the coefficients are found, the values $h_{i\pm\frac{1}{2}} = f_{i\pm\frac{1}{2}} + \mathrm{O}(\Delta x^k)$ can be computed and substituted into (17).

The scheme above is centralized at $x_{i+\frac{1}{2}}$ only if k is even, otherwise, it is shifted a half-cell to the left (upstream) or to the right (downstream). One often takes the upstream version of an odd order central scheme due to the inherent dissipation of upstream schemes, necessary to shock-capturing. For the sake of completeness, let us now take the case $k = 5$ and make the computations to obtain the fifth-order approximation to the spatial derivative in (17).

Thus, after substitution of a fourth-order polynomial in (16) and integration, we obtain

$$\hat{f}(x) = a_0 + a_1 x + a_2\left(x^2 + \frac{\Delta x^2}{12}\right) + a_3\left(x^3 + \frac{x\Delta x^2}{4}\right) + a_4\left(x^4 + \frac{x^2\Delta x^2}{2}\right), \tag{19}$$

which, if computed at the nodes $\{x_{i-2}, \ldots, x_{i+2}\}$ will determine the coefficients $\{a_0, \ldots, a_4\}$ in terms of $\{f_{i-2}, \ldots, f_{i+2}\}$, yielding

$$\hat{f}_{i+\frac{1}{2}} = \frac{1}{60}(2f_{i-2} - 13f_{i-1} + 47f_i + 27f_{i+1} - 3f_{i+2}), \tag{20}$$

and, analogously,

$$\hat{f}_{i-\frac{1}{2}} = \frac{1}{60}(2f_{i-3} - 13f_{i-2} + 47f_{i-1} + 27f_i - 3f_{i+1}). \tag{21}$$

Both are fifth-order approximations to $h_{i+\frac{1}{2}}$ and $h_{i-\frac{1}{2}}$, respectively:

$$\hat{f}_{i\pm\frac{1}{2}} = h_{i\pm\frac{1}{2}} - \frac{\Delta x^5}{60}\frac{\mathrm{d}^5 f}{\mathrm{d}x^5}\bigg|_{x=x_i} + \mathrm{O}(\Delta x^6). \tag{22}$$

The leading error order is the same for both stencils, so they will cancel out after substitution of (20) and (21) at (17), yielding a fifth-order approximation as pointed out beforehand.

3.2. WENO convex combination of stencils

The central finite difference scheme presented above will suffer from spurious oscillations if discontinuities are inside the interpolating stencils. The main idea of ENO schemes is to bias as much as necessary the central scheme to avoid the inclusion of the shock inside the stencil. For instance, a kth-order ENO approximation assigns smoothness weights to all k nodes stencils around the interpolating point and chooses the smoothest one to perform kth-order polynomial interpolations of the numerical flux.

Let us identify a particular stencil by its left-shift r. We have a polynomial interpolation to $h_{i+\frac{1}{2}}$ for each r, given by

$$\hat{f}_r(x_{i+\frac{1}{2}}) = \sum_{j=0}^{k-1} c_{rj} f_{i-r+j} = h(x_{i+\frac{1}{2}}) + \mathrm{O}(\Delta x^k), \tag{23}$$

where the c_{rj} are the Lagrangian interpolation coefficients [25]. The c_{rj} depend on the order k of the approximation and also on the left-shift parameter r, but not on the values f_i. Since r can vary from 0 to $k-1$, we have k distinct interpolating polynomials to choose from; all of them yielding a kth-order approximation, once f is smooth inside the intervals considered. The above process is called the reconstruction step, for it reconstructs the values of $h(x)$ at the cell boundaries of the interval $I_i = [x_{i-\frac{1}{2}}, x_{i+\frac{1}{2}}]$ from the cell average values $f(x)$ in the intervals $S_r = \{\bigcup_{j=0}^{k-1} I_{i-r+j},\ r = 0,\ldots,k-1\} = \{x_{i-r},\ldots,x_{i+s}\}$ with $s = k-r-1$.

However, at smooth regions, the collection of all k stencils carry information for an approximation of order higher than k. The weighted essentially non-oscillatory scheme (WENO) is an improvement over ENO for it uses a convex combination of all available polynomials for a fixed k, assigning zero weights to stencils containing discontinuities. This yields a $(2k-1)$ order scheme at smooth parts of the solution. The general WENO flux $\hat{f}_{i+\frac{1}{2}}$ is defined as

$$\hat{f}_{i+\frac{1}{2}} = \sum_{r=0}^{k-1} \omega_r \hat{f}_r\left(x_{i+\frac{1}{2}}\right), \tag{24}$$

where

$$\omega_r = \frac{\alpha_r}{\sum_{l=0}^{k-1}\alpha_l} \quad \text{with } \alpha_r = \frac{C_r}{(\varepsilon + IS_r)^p}. \tag{25}$$

Here, C_r are the ideal weights for the convex combination, the ones that at the absence of discontinuities provide a $(2r-1)$th order of approximation at (24) [25]; $\varepsilon = 10^{-10}$ is a small parameter to avoid division by zero, $p = 2$ is chosen to increase the difference of scales of distinct weights at non-smooth parts of the solution and IS_r is a measure of the smoothness of polynomials on the rth stencil:

$$\mathrm{IS}_r = \sum_{l=1}^{k-1} |\Delta x|^{2l-1} \int_{x_{i-\frac{1}{2}}}^{x_{i+\frac{1}{2}}} \left(\frac{\mathrm{d}^l}{\mathrm{d}x^l}\hat{f}_r(x)\right)^2 \mathrm{d}x. \tag{26}$$

When the interpolating polynomial on a given stencil is smooth, the smoothness indicator IS_r is relatively much smaller than those of stencils where the polynomial has discontinuities in its first $k-1$ derivatives. Therefore, discontinuous stencils receive a close to zero weight, $\alpha_r \approx 0$, and a non-oscillatory property is achieved.

Remark 1. There are different choices for the smoothness indicator IS_k and Taylor analysis reveals relevant properties of each of them. The first one was proposed in [25] and was based on divided differences. In [7], an improvement over (26) was proposed in order to increase the accuracy of the scheme at critical points (zero derivatives) of the smooth solution.

For a system of conservation laws such as the Euler equations, the eigenvectors and eigenvalues of the Jacobian of the flux are computed via the Roe Average method. Global Lax–Friedrichs flux splitting is used to split the flux into its positive and negative components. Artificial dissipation based on the modulus of the eigenvalues is added in order to obtain a smoother flux. The resulting positive and negative flux components are then projected into the characteristic fields using the left eigenvectors to form the positive and negative characteristic flux variables at each grid cell center. Then, high-order WENO polynomial reconstruction, as described above, is used to obtain these characteristic flux variables components at the grid cell boundaries, which, after summation, are finally projected back to physical space via the right eigenvectors. The details of this algorithm can be found in [25]. These characteristic flux variables projections are the expensive part of the WENO scheme when applied to systems of equations. They are necessary because high order approximation is not achieved within the framework of the conservative variables. A hybrid Spectral-WENO scheme would save substantial computational effort by avoiding the characteristic projections at all smooth parts of the solution.

4. Multi-resolution analysis

The successful implementation of the hybrid method depends on the ability to obtain accurate information on the smoothness of a function. In this work, we employ the multi-resolution (MR) algorithms by Harten

[23,24] to detect the smooth and rough parts of the numerical solution. The general idea is to generate a coarser grid of averages of the point values of a function and measure the differences (MR coefficients) d_i between the interpolated values from this sub-grid and the point values themselves. A tolerance parameter ϵ_{MR} is chosen in order to classify as smooth those parts of the function that can be well interpolated by the averaged function and as rough those where the differences d_i are larger than the parameter ϵ_{MR}. We shall see that the order of interpolation is relevant and the ratio between d_i of distinct orders may also be taken as an indication of smoothness.

Let us start by showing two examples where one can notice the detection capabilities of the multi-resolution analysis that will be presented below. The left and right figures of Fig. 4 show the piecewise analytic function

$$f(x) = \begin{cases} 10 + x^3 & -1 \leqslant x < -0.5, \\ x^3 & -0.5 \leqslant x < 0, \\ \sin(2\pi x) & 0 \leqslant x \leqslant 1, \end{cases} \tag{27}$$

and the density (ρ) of the Mach 3 shock-entropy wave interaction problem [25], as computed by the classical fifth-order WENO finite difference scheme, respectively.

The test function (27) has a jump discontinuity at $x = -0.5$ and a discontinuity at its first derivative at $x = 0$. One can see that at each grid point the differences d_i decay exponentially to zero inside the analytical pieces of the function when the order of interpolation increases from $n_{\mathrm{MR}} = 3$ to $n_{\mathrm{MR}} = 8$. At the discontinuity $x = 0.5$, the measured differences d_i are O(1) and remain unchanged despite the increase of the interpolation order. Similar behavior is exhibited at the derivative discontinuity at $x = 0$ with a smaller amplitude.

Also, in the right figure of Fig. 4, the density of the Mach 3 shock-entropy wave interaction problem and the corresponding MR coefficients d_i are shown for the third, fifth and seventh-order multi-resolution analysis. The location of the main shock is at $x \approx 2.73$ and the shocklets behind the main shock are well captured. The high frequencies behind the main shock are much better distinguished with the higher orders.

Averaging a function corresponds to filtering the upper half of the spectrum. The main idea of Hartens smoothness classification is to measure how distant the actual values of the function are from being predicted through interpolation of the lower half of the frequencies contained in the sub-grid of averages. We now describe a detailed construction of the sub-grid of averages and its corresponding interpolating polynomial, finishing with a worked example.

Given an initial number of grid points N_0 and grid spacing Δx_0, consider the set of nested dyadic grids $\{G^k, 0 \leqslant k \leqslant L\}$, defined as

$$G^k = \{x_i^k, i = 0, \ldots, N_k\}, \tag{28}$$

where $x_i^k = i\Delta x_k$, $\Delta x_k = 2^k \Delta x_0, N_k = 2^{-k} N_0$. For each level $k > 0$ we define the set of cell averages $\{\bar{f}_i^k, i = 1, \ldots, N_k\}$ at x_i^k of a function $f(x)$:

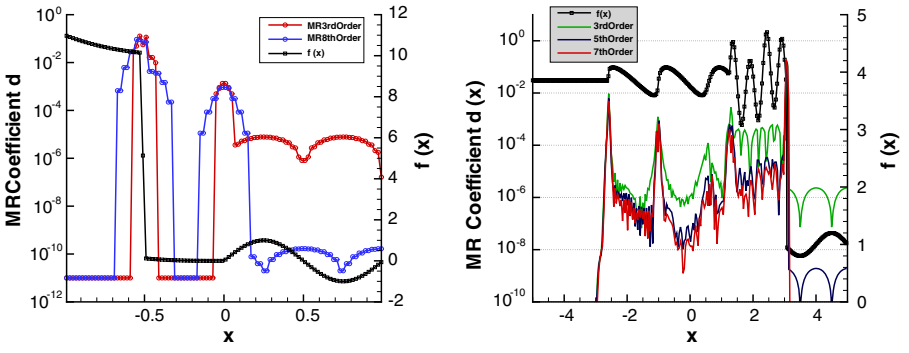

Fig. 4. (Left) The third and eighth-order MR coefficients d_i of the piecewise analytic function. (Right) The third, fifth and seventh-order MR coefficients d_i of the density $f(x) = \rho$ of the Mach 3 shock-entropy wave interaction problem.

$$\bar{f}_i^k = \frac{1}{\Delta x_k}\int_{x_{i-1}^k}^{x_i^k} f(x)\,dx, \tag{29}$$

and $\bar{f}_i^0 = f_i^0$. Let $\tilde{f}_{2i-1}^k$ be the approximation to $\bar{f}_{2i-1}^k$ by the unique polynomial of degree $2s$ that interpolates $\bar{f}_{i+l}^k, |l| \leqslant s$ at x_{i+l}^k, where $r = 2s+1$ is the order of approximation.

The approximation differences, also called multi-resolution coefficients, $d_i^k = \bar{f}_{2i-1}^{k-1} - \tilde{f}_{2i-1}^{k-1}$, at the kth grid level and grid point x_i, have the property that if $f(x)$ has $p-1$ continuous derivatives and a jump discontinuity at its pth derivative, then

$$d_i^k \approx \begin{cases} \Delta x_k^p [f_i^{(p)}] & \text{for } p \leqslant r \\ \Delta x_k^r f_i^{(r)} & \text{for } p > r \end{cases}, \tag{30}$$

where $[\cdot]$ denotes the magnitude of the jump of the function inside.

From formula (30) it follows that

$$|d_{2i}^{k-1}| \approx 2^{-\bar{p}} |d_i^k|, \quad \text{where } \bar{p} = \min\{p, r\}. \tag{31}$$

Eq. (31) shows that away from discontinuities, the MR coefficients d_i^k diminish in size with the refinement of the grid; close to discontinuities, they remain the same size, independent of k. The MR coefficients d_i^k were used in [24] in two ways. Firstly, finer grid data $\bar{f}_i^0$ were mapped to its M level multi-resolution representation $\bar{f}_i^0 = (d_i^1, \ldots, d_i^M, \bar{f}_i^M)$ to form a multi-scale version of a particular scheme, where truncation of small quantities with respect to a tolerance parameter decreased the number of flux computations. Secondly, the MR coefficients d_i^k also acted as a shock detection mechanism and an adaptive method was designed where a second-order Lax–Wendroff scheme was locally switched to a first-order accurate TVD Roe scheme, whenever d_i^1 was bigger than ϵ_{MR}.

Eq. (30) also indicates that the variation of the MR order, n_{MR}, can give additional information on the type of the discontinuity. Nevertheless, in this work, we will be limited at using only the first level $k = 1$ of the multi-resolution coefficients and we shall drop the superscript 1 from here on.

Hence, to find d_i, the idea is to construct a piecewise polynomial $P_k(x)$ of degree $k = n_{\mathrm{MR}}$ using $k+1$ computed average values of f_i, $\bar{f}_i$, at the equi-spaced grid x_i such that

$$P_k(x_i) = f(x_i) + \mathrm{O}(\Delta x^{k+1}), \tag{32}$$

and

$$d_i = f_i - P_k(x_i). \tag{33}$$

Given a tolerance level ϵ_{MR}, the smoothness of the function $f(x)$ at x_i would then be checked against the magnitude of the d_i, namely:

$$\begin{cases} |d_i| \leqslant \epsilon_{\mathrm{MR}} & \Rightarrow \text{solution is smooth.} \\ |d_i| > \epsilon_{\mathrm{MR}} & \Rightarrow \text{solution is non-smooth.} \end{cases} \tag{34}$$

The algorithm for computing the MR coefficients d_i is given next.

4.1. Computing the MR coefficients

Consider an equi-spaced grid $\{x_i = i\Delta x,\ i = -m, \ldots, 0, \ldots, N, \ldots, N+M\}$, where Δx is the constant grid spacing. N can be an odd or an even number. Depending on N and the even or odd order of the MR analysis n_{MR}, the number of ghost points m and M required are given in Table 1.

Table 1
The number of ghost points m and M required for the MR Analysis

N	Odd	Even	Odd	Even
n_{MR}	Odd	Odd	Even	Even
m	$n_{\mathrm{MR}}+1$	$n_{\mathrm{MR}}+1$	n_{MR}	n_{MR}
M	$n_{\mathrm{MR}}+1$	n_{MR}	$n_{\mathrm{MR}}+2$	$n_{\mathrm{MR}}+1$

Given the grid point values of the function $f(x)$, the average values are computed as

$$\bar{f}_i = \frac{1}{2}(f_{2i} + f_{2i+1}), \quad i = -\frac{m}{2}, \ldots, \frac{N+M-1}{2}. \tag{35}$$

We construct a piecewise $k = n_{MR}$ degree polynomial $P_k(x)$ using the $k+1$ computed average values of the given function, $\bar{f}_i$ such that

$$P_k(x_i) = f(x_i) + \mathrm{O}(\Delta x^{k+1}). \tag{36}$$

The polynomial $P_k(x_i)$, $l = \frac{1}{2}m$ and $L = l - 1$ or $L = l$ if k is odd or even, respectively, can be written as

$$P_k(x_i) = \sum_{r=i-l}^{i+L} \alpha_r \bar{f}_r. \tag{37}$$

However, since the coefficients α depend only on x_i and do not depend on the function $f(x)$, the $P_k(x_i)$ can be written as

$$P_k(x_i) = \begin{cases} \sum_{r=-l}^{L} \alpha_r \bar{f}_{i+r}, & \mathrm{mod}(i,2) = 0 \\ \sum_{r=-l}^{L} \beta_{r+1} \bar{f}_{i+r}, & \mathrm{mod}(i,2) = 1 \end{cases}. \tag{38}$$

In the case of $\mathrm{mod}(i,2) = 1$.

$$\beta_{-r} = \alpha_r, \quad r = -l, \ldots, L. \tag{39}$$

Furthermore, if n_{MR} is even, the coefficients α are symmetric about $r = 0$, namely, $\alpha_{-r} = \alpha_r$, $r = 1, \ldots, L$.

The desired coefficients α are computed by requiring $P_k(x)$ to be equal to each of the first $k+1$ monomials $f(x) = 1, x, x^2, \ldots, x^k$ and evaluated at any grid point $x = x^*$. For simplicity, we take $x^* = 0$. The $\bar{f}_i$ are evaluated for $i = -l, \ldots, L$. This procedure results in a system of $(L+l+1) \times (L+l+1)$ linear equations, $\mathbf{A}\vec{\alpha} = \vec{b}$, where

$$\mathbf{A} = \begin{pmatrix} 1 & \ldots & 1 \\ -2l + (-2l+1) & \ldots & 2L + (2L+1) \\ \vdots & \vdots & \vdots \\ (-2l)^k + (-2l+1)^k & \ldots & (2L)^k + (2L+1)^k \end{pmatrix}, \tag{40}$$

and

$$\vec{\alpha} = \begin{pmatrix} \alpha_{-l} \\ \alpha_{-l+1} \\ \vdots \\ \alpha_L \end{pmatrix}, \quad \vec{b} = \begin{pmatrix} 1 \\ 0 \\ \vdots \\ 0 \end{pmatrix},$$

Using (38), the kth-order multi-resolution coefficients d_i at x_i can be computed as

$$d_i = f_i - P_k(x_i), \quad i = 0, \ldots, N. \tag{41}$$

One can also evaluate the α by matching the terms in the Taylor series expansion using (36) and (37) to any desired order, however this procedure may become cumbersome for high order k.

Example. To illustrate the procedure above, we will construct two unique local polynomials with $k = n_{\mathrm{MR}} = 3$, such that $P_k(x_0) = f(x_0) + \mathrm{O}(\Delta x^{k+1})$ and $P_k(x_1) = f(x_1) + \mathrm{O}(\Delta x^{k+1})$.

To construct the desired polynomials one needs to find the unique coefficients $\{\alpha_{-2}, \alpha_{-1}, \alpha_0, \alpha_1\}$ and $\{\beta_{-1}, \beta_0, \beta_1, \beta_2\}$ such that

$$\alpha_{-2}\bar{f}_{-2} + \alpha_{-1}\bar{f}_{-1} + \alpha_0\bar{f}_0 + \alpha_1\bar{f}_1 = f(x_0) + \mathrm{O}(\Delta x^4) \tag{42}$$

and

$$\beta_{-1}\bar{f}_{-1} + \beta_0\bar{f}_0 + \beta_1\bar{f}_1 + \beta_2\bar{f}_2 = f(x_1) + \mathrm{O}(\Delta x^4). \tag{43}$$

The system of Eq. (40), becomes

$$\mathbf{A} = \begin{pmatrix} 1 & 1 & 1 & 1 \\ -7 & -3 & 1 & 5 \\ 25 & 5 & 1 & 13 \\ -91 & -9 & 1 & 35 \end{pmatrix}, \quad \vec{\alpha} = \begin{pmatrix} \alpha_{-2} \\ \alpha_{-1} \\ \alpha_0 \\ \alpha_1 \end{pmatrix}, \quad \vec{b} = \begin{pmatrix} 1 \\ 0 \\ 0 \\ 0 \end{pmatrix}. \tag{44}$$

Solving this system yields

$$\alpha_{-2} = -\frac{3}{64}, \quad \alpha_{-1} = \frac{17}{64}, \quad \alpha_0 = \frac{55}{64}, \quad \alpha_1 = -\frac{5}{64}, \tag{45}$$

and $\{\beta_{-1} = \alpha_1, \beta_0 = \alpha_0, \beta_1 = \alpha_{-1}, \beta_2 = \alpha_{-2}\}$.

Remark 2. The tolerance parameter ϵ_{MR} determines the dynamic activation of the spectral and WENO spatial discretizations along the various subdomains of the hybrid method. While a too small value of ϵ_{MR} activates the more expensive WENO method at subdomains where the solution is smooth, a larger value activates the spectral method at a subdomain with low spatial resolution, generating oscillations. ϵ_{MR} also bears a straight relation with the interpolation order n_{MR}. High n_{MR} values decrease the size of ϵ_{MR} one needs to chose, since high frequencies are less mistaken by gradient jumps. The general guideline is to start with a value for n_{MR} at least equal to the order of the WENO method and increase it according to the complexity of the solution. For instance, $n_{\mathrm{MR}} = 5$ is a good choice for the piecewise smooth solution of the SOD problem, the Entropy problem would work better with $n_{\mathrm{MR}} = 7$. For most of the flows with shock that were tested, the value of $\epsilon_{\mathrm{MR}} = 10^{-3}$ yielded a good balance between computational speed and accuracy of the numerical solution.

5. The multi-domain hybrid spectral–WENO method

The main idea is straightforward: Partition the physical domain into equal sized subdomains, avoid Gibbs phenomenon by treating discontinuities with essentially non-oscillatory shock capturing WENO methods and increase the numerical efficiency by treating the smooth parts of the solution with spectral methods.

In the case of a stationary discontinuity, one only needs appropriate interface conditions to transmit data between the subdomains. A moving shock situation requires in addition a smoothness measurement routine to keep track of the high gradients and also a subdomain switching algorithm in order to change spectral domains to WENO ones, once the shock gets closer to them, and switch back WENO subdomains to spectral ones, once the shock leaves them. These same tools will do the work in the case when discontinuities are being created in spectral subdomains, as we shall see later in Section 6, when we simulate the interaction of a Mach 3 shock with a sinusoidal density wave. In this section we describe the necessary treatment of the interfaces between the subdomains and the algorithm used to switch the type of a subdomain, from WENO to spectral and vice versa.

5.1. Interfaces treatment

One of the main components of the Hybrid scheme is the exchange of information at the interfaces between subdomains that might be of distinct types. The correct setting of these interfaces is of great relevance in order to avoid loss of accuracy or numerical oscillations that could contaminate the solution. The Hybrid scheme deals with three types of such interfaces, namely,

(1) Spectral–spectral interface;
(2) Spectral–WENO interface;
(3) WENO–WENO interface.

We shall denote the grid points of the left and right subdomains by x and y, respectively. The functional values at these points are denoted by S and W for spectral and WENO subdomains, respectively. N_S and N_W are the number of Chebyshev collocation points of the spectral grid and the number of uniformly spaced grid points of the WENO subdomain, respectively.

5.2. Spectral–spectral interface

At a spectral–spectral interface the solution is assumed to be smooth, otherwise the switching algorithm presented in the next subsection would had already changed the subdomains to WENO. This fact, along with the high order accuracy of the spectral solutions in each subdomain $\mathbf{k}$, ensures that a simple average of the two functional values is sufficient for obtaining continuity of the solution across the interface, that is

$$s_0^{\mathbf{k}} = s_{N_S}^{\mathbf{k}+1} = \frac{1}{2}(s_0^{\mathbf{k}} + s_{N_S}^{\mathbf{k}+1}). \tag{46}$$

Other types of interface conditions, such as the imposition of the solution of the Riemann problem at the spectral–spectral interface, yielded no discernible differences in the cases tested.

5.3. Spectral–WENO interface

At a spectral–WENO (WENO–spectral) interface, the ghost points of the WENO grid $\{y_{-r},\ldots,y_{-1}\}$, where r is the number of WENO ghost points, in the subdomain $\mathbf{k}$, are inside the spectral subdomain $\mathbf{k}-1$; and the end point of the spectral subdomain $\mathbf{k}-1$, x_0, is in between the first ghost point y_{-1} and the first interior point y_0 of the WENO grid in subdomain $\mathbf{k}$. The spectral point and all the WENO ghost points need to be adjusted for continuity of the solution at the interface. The idea is to use information of the spectral subdomain to interpolate at the ghost points and, after that, to interpolate the spectral boundary point using the surrounding WENO grid points:

- The solution values at the ghost points of the WENO subdomain are computed via spectral interpolation using the data $(s(x_0),\ldots,s(x_{N_S}))$ of the spectral subdomain. That is,

$$w(y_i) = \sum_{j=0}^{N_S} s(x_j) g_j(y_i), \quad i = -r,\ldots,-1, \tag{47}$$

  where $g_j(x)$ is the Lagrangian interpolation polynomial of degree N_S (see Eq. (5)).
- The functional value of the spectral grid at x_0 is obtained through a polynomial interpolation using the functional values of the interior points and the updated ghost points of the WENO subdomain. The degree of the interpolating polynomial should match the order of the WENO method.

The hierarchy of interpolation above does matter. We first generate the ghost points of the WENO grid because these are inside the spectral subdomain and, therefore, must agree with the spectral solution. Generating the spectral endpoint x_0 at first would use wrong information from the ghost points. The case of a WENO–spectral interface is completely analogous and one should also respect the same interpolation hierarchy as above: ghost points first.

5.4. WENO–WENO interface

It will be through the interface between WENO subdomains where possible discontinuities in the solution are going to be transmitted. In [17], numerical experiments show that WENO or Lagrangian interpolation are not conservative if the neighboring subdomains have different grid spacing Δx and that, once this condition is satisfied, both interpolations are conservative and behave equivalently. In this work, we only consider WENO subdomains with the *same grid spacing* Δx in order to avoid such complications. This restriction also makes ghost points of a subdomain to coincide with interior points of the neighboring subdomain and, for practical

matters, both subdomains can be treated as a single larger subdomain with no interface, allowing shocks to pass through as if they were "walking" at interior points of a WENO discretization. If we denote by w^{L} and w^{R} the functional values of the left and right WENO subdomains, respectively, we have:

$$\begin{cases} w^{\mathrm{L}}_{N_{\mathrm{W}}+i} = w^{\mathrm{R}}_{i} \\ w^{\mathrm{R}}_{-i} = w^{\mathrm{L}}_{N_{\mathrm{W}}-i} \end{cases}, \quad i = 1, \ldots, r, \tag{48}$$

where N_{W} and the size of the adjacent WENO subdomains are assumed to be the same.

Example. Let us now show by means of a numerical example that the hybrid method with the above interface conditions is an improvement over the classical WENO scheme. Consider the inviscid Burgers equation

$$\begin{cases} u_t + \frac{1}{2}(u^2)_x = 0 \quad -1 < x < 1, \\ u(x,0) = 0.3 + 0.7\sin(\pi x), \end{cases} \tag{49}$$

with periodic boundary conditions. The initial configuration will quickly evolve into a moving shock. At this point, however, we will analyze the pre-shock error in order to show that the superior accuracy of the spectral scheme improves the WENO error as we see in Fig. 5. For the classical WENO method, we discretize the interval $[-1,1]$ with 400 points. For the Hybrid method, the interval is subdivided into three equal sized subdomains, where the middle one, $[-0.3,0.3]$, is a spectral subdomain. The subdomains configuration is kept fixed, since no shock will arise during the time interval of the experiment.

The number of points in the WENO subdomains are the same as the corresponding regions of the classical WENO, so any increase of accuracy must be due to the spectral subdomain. Note that not only the error at the spectral subdomain is smaller than the one of the classical WENO, but it also forces the decreasing of the overall error, showing its superior performance and also the conservation properties of the interface conditions. Another aspect that should be noticed is the globality of the spectral scheme that can be observed when looking to the uniformity of the error at the spectral subdomain.

5.5. The switching algorithm

In this section, we describe the subdomain switching algorithm. Since we are interested in solving unsteady moving shocked flows, the subdomains must be able to switch from one type of subdomain to the other, as dictated by the smoothness of the solution and determined by the multi-resolution analysis of Section 4.

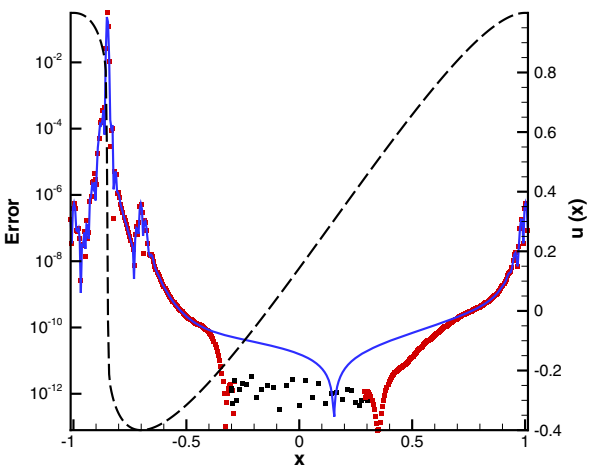

Fig. 5. (Dashed line) Inviscid Burgers equation solution; (continuous line) error of the fifth-order classical WENO with 400 points; (symbols) error of the Hybrid method.

Each WENO subdomain must have a "Buffer Area" in order to detect outgoing shocks or high gradients and "warn" the immediate neighboring spectral subdomains to switch to WENO type. The "Buffer Area" for a given WENO subdomain is defined as two sets of grid points at either ends of the subdomain, namely, $B_0 = \{x_0, \ldots, x_{N_B}\}$ and $B_1 = \{x_{N_W} - N_B + 1, \ldots, x_{N_W}\}$. As greater as is the value of the number of ghost points, N_B, earlier is the detection of shocks and gradients, however, at the cost of earlier switching of the adjacent spectral subdomains and greater chance of unnecessary costly computations. Satisfactory results have been obtained with the default value $N_B = r$, the number of ghost cells used in the given order of the WENO scheme in this study. It should be noted that the grid points in the "Buffer Area" are part of the interior grid points and should not be confused with the WENO ghost points.

For the switching algorithm, the three conditions below are the main rules to be followed:

(1) If a subdomain contains high gradients, then switch its spatial discretization to (or keep it as) WENO.
(2) If high gradients are present in the "Buffer Areas" of neighboring subdomains, then switch the current subdomain to (or keep it as) a WENO subdomain.
(3) In any other case, switch the subdomain to (or keep it as) a spectral subdomain.

The first condition above avoids the Gibbs phenomenon, keeping the discontinuities inside WENO subdomains. The second condition ensures the switching of a spectral subdomain to a WENO one in order to allow only WENO-to-WENO transmission of high gradients. The third condition improves the numerical efficiency, since it ensures that smooth parts of the solution will always be contained in spectral subdomains.

Multi-resolution analysis of the solution is performed at the beginning of every step of the associated temporal scheme, in our case, a third-order Runge–Kutta scheme, as described in Section 6 below. At each subdomain $\mathbf{k}$, we define the smoothness flag variable, $\mathrm{Flag}_i^{\mathbf{k}}$, at each grid point x_i excluding the ghost points, as

$$\mathrm{Flag}_i^{\mathbf{k}} = \begin{cases} 1, & |d_i^{\mathbf{k}}| > \epsilon_{\mathrm{MR}} \\ 0, & \text{otherwise} \end{cases}, \quad i = 0, \ldots, N_W, \tag{50}$$

where $d_i^{\mathbf{k}}$ are the MR coefficients. Since the multi-resolution analysis requires uniformly spaced grids, the spectral grids are first interpolated to uniformly spaced grids before obtaining the MR coefficients $d_i^{\mathbf{k}}$. The necessary ghost points are acquired from the neighboring subdomains. At the boundary subdomains, the values of the boundary ghost points are extrapolated linearly from the interior data.

The algorithm proceeds by checking for each spectral subdomain $\mathbf{k}$ and at the Buffer Areas of the neighboring subdomains $\mathbf{k}-1$ and $\mathbf{k}+1$, if any of $\{\mathrm{Flag}_i^{\mathbf{k}}, i = 0, \ldots, N_W\}$, $\{\mathrm{Flag}_i^{\mathbf{k}+1}, i = 0, \ldots, N_B\}$ or $\{\mathrm{Flag}_i^{\mathbf{k}-1}, i = N_W - N_B + 1, \ldots, N_W\}$ is equal to one. If so, it switches subdomain $\mathbf{k}$ to a WENO discretization. Otherwise, a spectral discretization is implemented, or kept. These switches require the use of interpolation from a Chebyshev grid to a uniformly spaced one and vice-versa:

- To switch from the spectral subdomain to the WENO subdomain, the data are interpolated onto the uniformly spaced grid via the spectral interpolation formula.
- To switch from the WENO subdomain to the spectral subdomain, the data are interpolated onto the Chebyshev Gauss–Lobatto points via the Lagrangian interpolation polynomial of the same order as the WENO method.

Remark 3. Back and forth switching between WENO and spectral discretizations may occur too frequently for the same domain when the ϵ_{MR} is marginally set. The $d_i^{\mathbf{k}}$ coefficients might oscillate around the parameter ϵ_{MR} in time due to some numerical factors such as dissipation, dispersion and nonlinear effects, or any combination of such. This pattern of switching can repeat itself for a while until the solution settles down with a clear definition of the $d_i^{\mathbf{k}}$, which is either greater than or smaller than the MR tolerance ϵ_{MR}. In order to alleviate such occurrences, one must devise a procedure preventing the switch from WENO to spectral if it had already occurred recently. However, such procedure must never prevent a spectral to WENO switch, for oscillations and instability might occur.

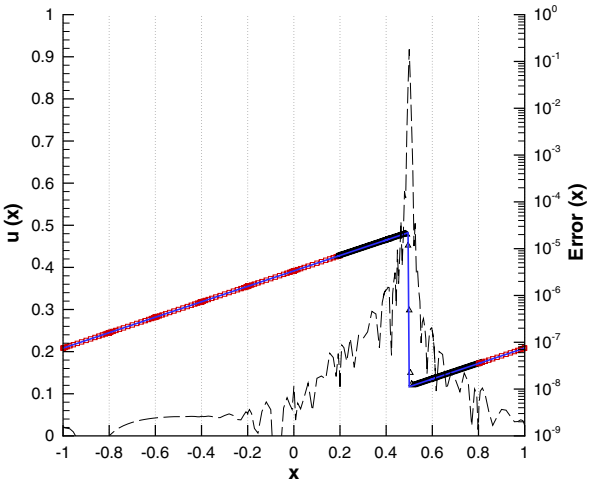

Fig. 6. Inviscid Burgers equation solution. The solution computed by the Hybrid scheme is plotted with symbols against the exact solution in solid line. The error is plotted in dashed lines. Vertical dashed lines show the subdomains division. Subdomains $[0.2, 0.4]$, $[0.4, 0.6]$ and $[0.6, 0.8]$ are WENO, all others are spectral.

We end this section proceeding further with the temporal integration of the inviscid Burgers Eq. (49) to a final time $t = 5$ where the shock has already developed and performed an entire revolution at the periodical domain. The numerical results are shown at Fig. 6 where we now have partitioned the interval with 10 subdomains. Each spectral subdomain uses 17 points, while the WENO ones use 40 points. Note that the Hybrid Method was able to compute the exact location of the shock, demonstrating its conservative property.

6. Numerical experiments

In this section, we present numerical experiments with the system of Euler equations for gas dynamics in strong conservation form:

$$\mathbf{Q}_t + \mathbf{F}_x = 0, \tag{51}$$

where

$$\mathbf{Q} = (\rho, \rho u, E)^{\mathrm{T}}, \quad \mathbf{F} = (\rho u, \rho u^2 + P, (E + P)u)^{\mathrm{T}}, \tag{52}$$

and the equation of state

$$P = (\gamma - 1)\left(E + \frac{1}{2}\rho u^2\right), \quad \gamma = 1.4. \tag{53}$$

In all examples below, the physical domain is partitioned into a fixed number of same size subdomains and the initial configuration of these subdomains depends on the initial condition under consideration. Spectral subdomains are discretized with Chebyshev–Gauss–Lobatto collocation points and WENO subdomains use an uniform grid, where the classical fifth-order characteristic-wise WENO finite difference is applied. We shall use the same number of uniformly spaced grid points N_{W} for all WENO subdomains, as well as the same number of Chebyshev collocation points N_{S} at all spectral subdomains, unless noted otherwise. The detection of discontinuities and high gradients is performed through a fifth-order multi-resolution analysis applied to the density function ρ. A 16th-order Exponential filter is employed in all spectral subdomains.

To evolve in time the ODEs resulting from the semi-discretized PDEs, the third-order total variation diminishing Runge–Kutta scheme (RK-TVD) will be used [25]:

$$\begin{aligned}\vec{U}^1 &= \vec{U}^n + \Delta t L(\vec{U}^n)\\ \vec{U}^2 &= \frac{1}{4}(3\vec{U}^n + \vec{U}^1 + \Delta t L(\vec{U}^1)),\\ \vec{U}^{n+1} &= \frac{1}{3}(\vec{U}^n + 2\vec{U}^2 + 2\Delta t L(\vec{U}^2)),\end{aligned} \tag{54}$$

where L is the spatial operator. CFL numbers for the spectral and WENO subdomains are set to be 1 and 0.4, respectively. All results of the hybrid method are compared with an exact solution or with a numerical solution obtained with the classical WENO scheme with the same spatial resolution of the hybrid scheme. This is achieved by using the same number of points for the classical scheme as if all subdomains in the hybrid were of the WENO type (see Section 5). The main goal of the numerical experiments below is to show that the Hybrid method obtains equivalent solutions as the classical WENO scheme, however at a lower computational cost. This is easily concluded from the facts that spectral discretization is much more efficient than the finite differences at smooth parts of the solution and that spectral subdomains avoid the expensive characteristic decomposition of the WENO scheme.

In the figures shown for the one dimensional test cases, the spectral and WENO subdomains are those denoted with squares (□) and triangles (△) symbols respectively. The subdomains are also indicated by vertical dashed lines and major ticks on the x axis. Under each figure, the subdomains configuration is indicated as a sequence of powers of S and W, where the exponent means the number of consecutive subdomains of the same type. This notation will make easier the counting of subdomain types when a large number of subdomains is used.

6.1. SOD problem

We first consider the Sod problem of the Euler equations with initial Riemann data:

$$(\rho, U, P) = \begin{cases} (0.125, 0, 0.1) & -5 \leqslant x < 0,\\ (1, 0, 1) & 0 \leqslant x < 5.\end{cases} \tag{55}$$

The physical domain $[-5,5]$ is partitioned into five equal subdomains. Since the initial condition is discontinuous at the center of the physical domain, the middle subdomain, $[-1,1]$, is set as WENO (Fig. 7(a)). Here, $N_S = 16$ and $N_W = 110$ and the MR tolerance was taken as $\epsilon_{MR} = 5 \times 10^{-3}$.

As time evolves, the initial density discontinuity develops into two jump discontinuities, the leftward moving shock front and contact discontinuity and a rightward moving rarefaction wave, which is discontinuous in the first derivative (Figs. 7(b) and (c)). Notice that when the discontinuities move on closer to the boundary of the WENO subdomain $[-1,1]$, the neighboring spectral subdomains are switched to WENO ones. At a later time, the discontinuities had moved further to the left side of the physical domain, however the first and last subdomains were kept as spectral ones, since none of them had been yet "threatened" by the discontinuities.

6.2. 123 problem

We now consider the 123 problem with initial Riemann data,

$$(\rho, U, P) = \begin{cases} (1, -2, 0.4) & -5 \leqslant x < 0,\\ (1, 2, 0.4) & 0 \leqslant x \leqslant 5.\end{cases} \tag{56}$$

The solution consists of two rarefaction waves moving in opposite directions which are generated at the center of the physical domain by a discontinuity in the velocity.

Using the same setting as the Sod problem discussed in the previous example, we compute the numerical solution up to $t = 1$. Fig. 8(d) shows that the middle WENO subdomain $[-1,1]$ is switched to spectral as soon as the rarefaction waves move away from the buffer zones of the neighboring domains. Note also that the first and last spectral subdomains have a smaller number of discretization points than the newly created spectral subdomain, showing that the Hybrid scheme might also provide quantitative flexibility at the local discretizations. Non-consecutive WENO subdomains can also have distinct number of grid points.

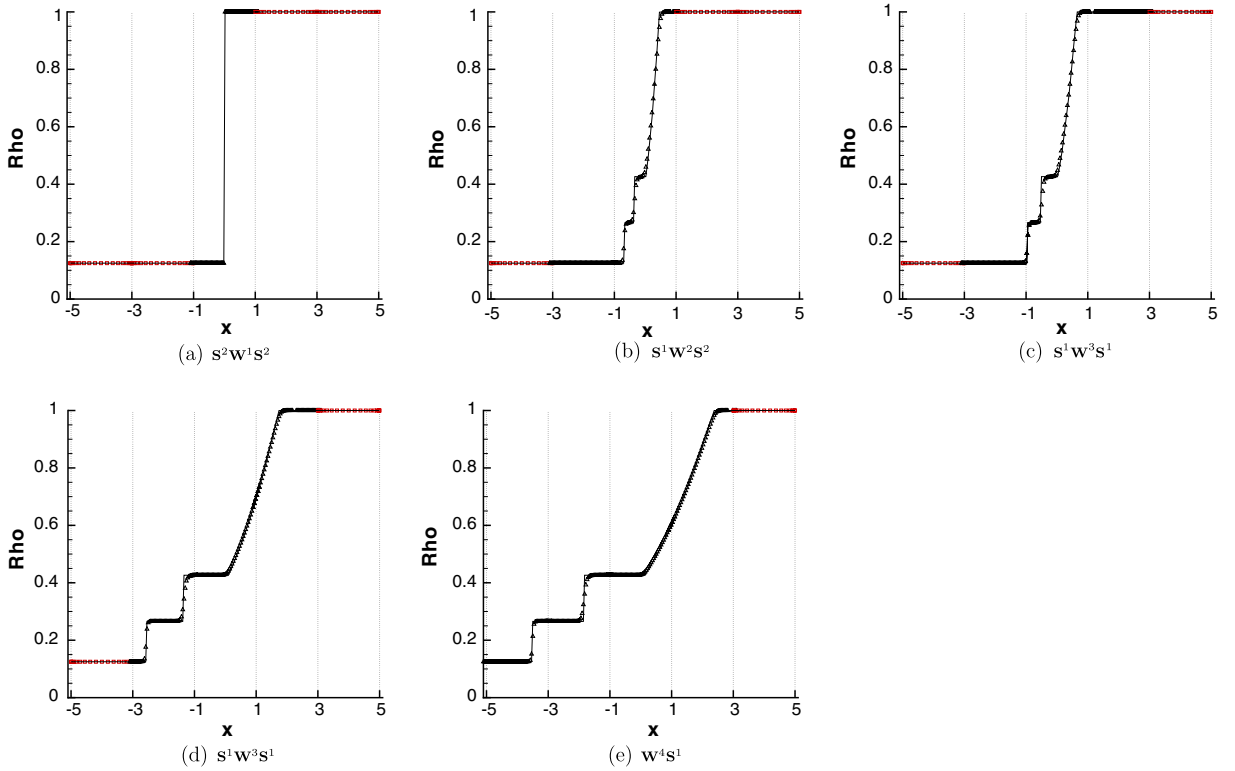

Fig. 7. The density profile of the Sod shock tube problem at times (a) $t = 0$, (b) $t = 0.39$, (c) $t = 0.54$, (d) $t = 1.46$ and (e) $t = 2$ with 5 subdomains. $N_S = 16$, $N_W = 110$ and $\epsilon_{MR} = 5 \times 10^{-3}$. Spectral (□); WENO (△); The solid line is the exact solution.

6.3. Blastwaves simulation

The one dimensional Blast waves interaction problem by Woodward and Collela [18] has the following initial profile

$$(\rho, U, P) = \begin{cases} (1, 0, 000) & 0 \leqslant x < 0.1 \\ (1, 0, 0.01) & 0.1 \leqslant x < 0.9 \\ (1, 0, 100) & 0.9 \leqslant x \leqslant 1.0 \end{cases}. \tag{57}$$

The initial pressure gradients generate two density shock waves that collide and interact later in time. In this experiment, the physical domain is subdivided into 10 subdomains and the number of Chebyshev collocation points and WENO uniform grid are $N_S = 16$ and $N_W = 50$, respectively. Reflective boundary conditions are applied at both ends of the physical domain. Fig. 9 shows that at the initial times, the expensive WENO discretizations are localized around the density peaks, while the remaining subdomains are spectral. At intermediate times, the left rarefaction wave spreads around, requiring the use of more WENO subdomains, however, by the end of the simulation, we have more spectral subdomains than WENO ones. It is clear from Fig. 9(c) that one could decrease the number of discretization points at the first five spectral subdomains, or take a step further and merge all the subdomains at a single spectral one, increasing the numerical efficiency of the algorithm. These improvements will be considered in future implementations of the Hybrid method.

6.4. Shock-entropy wave interaction

Consider the one dimensional Mach 3 shock-entropy wave interaction, specified by the following initial conditions:

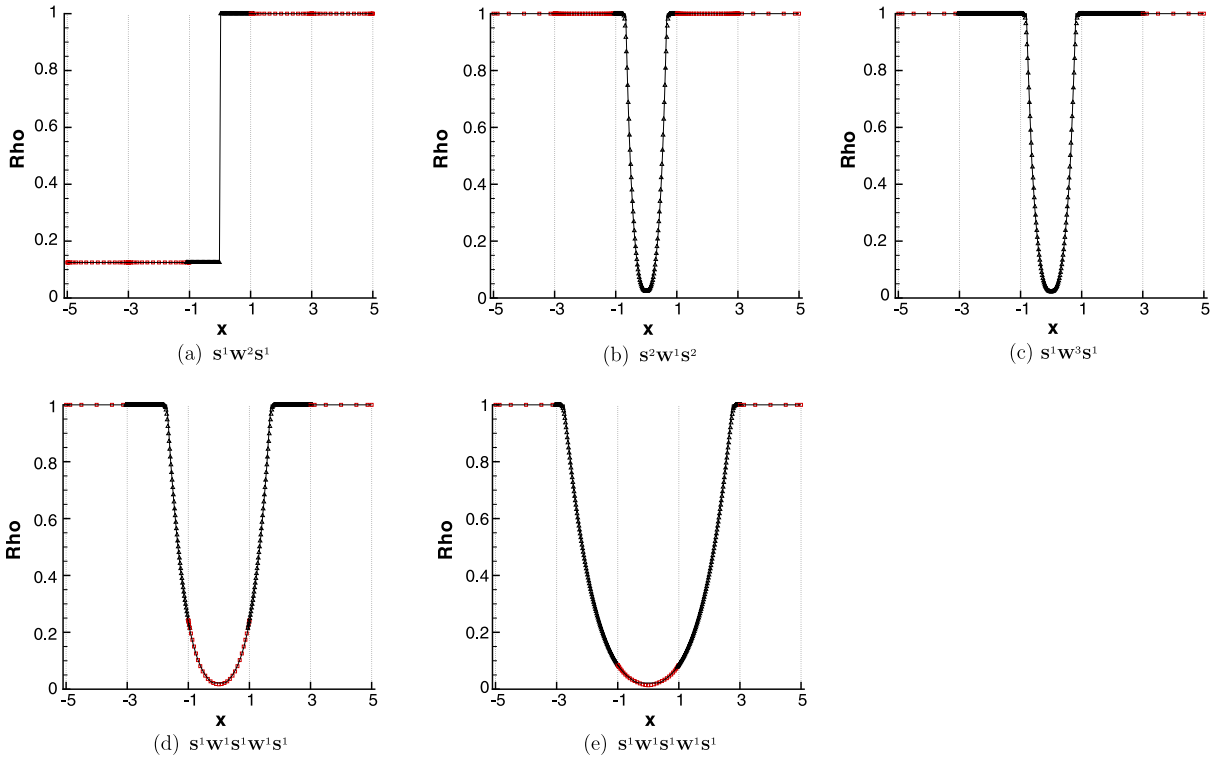

Fig. 8. The density profile of the 123 problem at times (a) $t = 0$, (b) $t = 0.25$, (c) $t = 0.29$, (d) $t = 0.62$ and (e) $t = 1$ with 5 subdomains. $N_S = 16$, $N_W = 110$ and $\epsilon_{MR} = 5 \times 10^{-3}$. Spectral (□); WENO (△); The solid line is the exact solution.

$$(\rho, u, P) = \begin{cases} (3.857143, 2.629369, 10.33333) & -5 \leqslant x < -4, \\ (1 + \epsilon \sin(kx), 0, 1) & -4 \leqslant x \leqslant 15, \end{cases} \tag{58}$$

where $x \in [-5, 15]$, $\epsilon = 0.2$ and $k = 5$. The solution of this problem consists of shocklets and fine scales structures which are located behind a right-going main shock. Fig. 10 shows that the hybrid method is able to capture all the smooth high frequency waves behind the main shock with spectral discretizations. Note that the WENO subdomains are located only at the main shock and at the steep gradients of the N-waves. The hybrid method uses 40 subdomains, with $N_S = 16$ and $N_W = 50$. The solid black line is the solution computed with

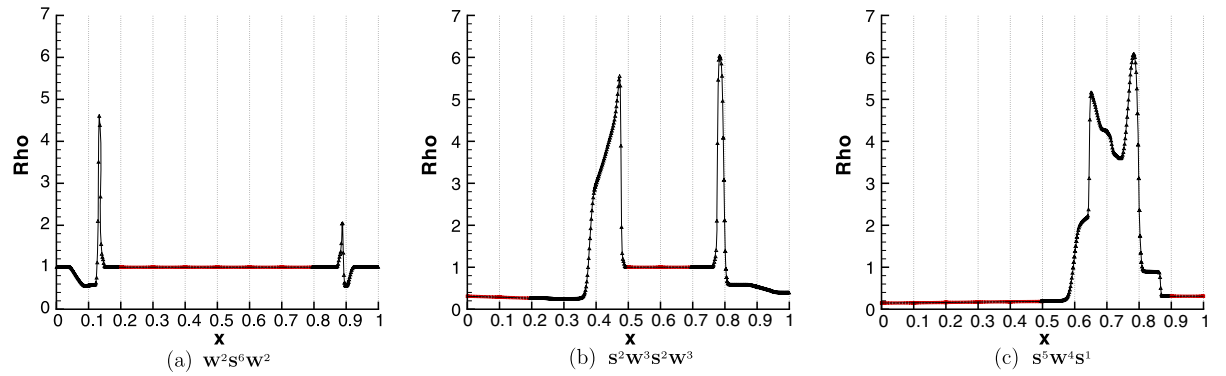

Fig. 9. The density profile of the Blastwave problem at times: (a) $t = 0.014$; (b) $t = 0.16$; and (c) $t = 0.38$ with 10 subdomains as indicated by the vertical dash lines, $N_S = 16$, $N_W = 50$ and $\epsilon_{MR} = 5 \times 10^{-3}$. Spectral (□); WENO (△); The solid line is the solution computed using the classical WENO scheme with 500 points.

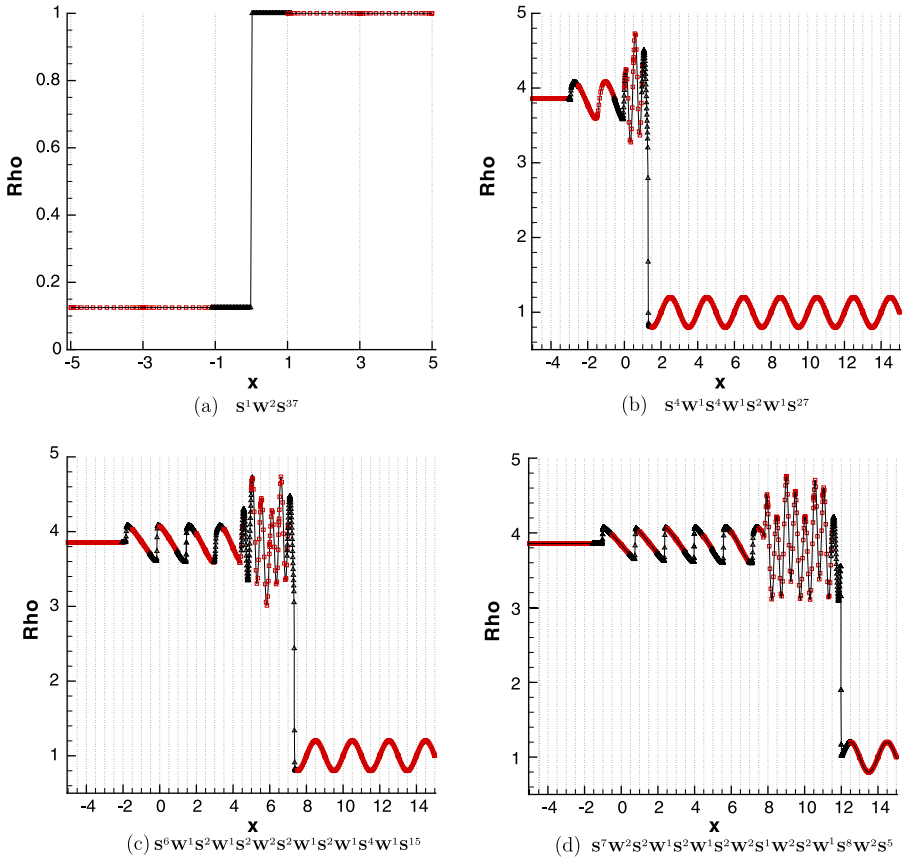

Fig. 10. The density profile of the Mach 3 shock-entropy wave interaction at times (a) $t = 0$, (b) $t = 1.5$, (c) $t = 3.2$ and (d) $t = 4.5$ with 40 subdomains, as indicated by the vertical lines. $N_S = 16$, $N_W = 50$ and $\epsilon_{MR} = 5 \times 10^{-3}$. Spectral (□); WENO (△). The solid line is the solution computed with the fifth-order WENO scheme with 2000 grid points.

the fifth-order WENO scheme with 2000 grid points. Fig. 10(d) also shows that even with the great complexity of the solution, less than 30% of the total number of subdomains are of the WENO type.

6.5. Shock-vortex interaction

We now show some previous results of the Hybrid method in more spatial dimensions. A more detailed discussion of the following two dimensional extension of the hybrid scheme can be found in [1]. In this experiment, the multi-domain hybrid configuration is applied to a 2D shock-vortex interaction. We consider a counter-clockwise rotating vortex centered at (x_c, y_c), and strength Γ, with a tangential velocity profile [9] given in polar coordinates by:

$$U(r) = \begin{cases} \Gamma r(r_0^{-2} - r_1^{-2}) & 0 \leqslant r \leqslant r_0 < r_1 \\ \Gamma r(r^{-2} - r_1^{-2}) & r_0 \leqslant r \leqslant r_1 \\ 0 & r > r_1 \end{cases}, \tag{59}$$

where $r_0 = 0.2$ and $r_1 = 1.0$. The physical domain ($0 \leqslant x \leqslant 3.9$, $-2 \leqslant y \leqslant 2$) is partitioned into a 13×10 grid of subdomains. Spectral and WENO subdomains use a 32×32 grid of Chebyshev collocation points and a 50×50 uniform grid, respectively. The multi-resolution analysis is performed with tolerance $\epsilon_{MR} = 5 \times 10^{-2}$.

We simulate a Mach 3 shock interacting with the vortex of strength $\Gamma = 0.25$ and compare the solution obtained by the hybrid method with the above setup with a highly resolved solution using the classical

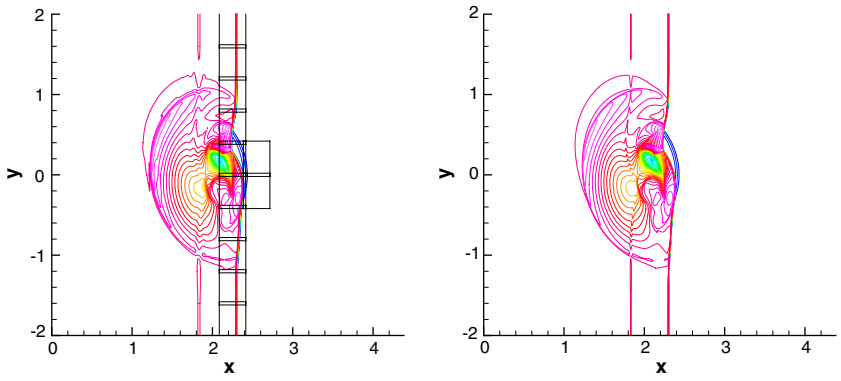

Fig. 11. Density contour of the shock-vortex interaction with Mach number $M_s = 3$ and vortex strength $\Gamma = 0.25$ at $t = 0.6$. Hybrid (left); Classical WENO (right). WENO subdomains are denoted by bounding boxes.

fifth-order characteristic-wise WENO finite difference scheme with a 1200×1200 grid at final time $t = 0.6$ (Fig. 11). The shock and the high gradient regions immediately behind the shock are well captured by the MR analysis, as indicated by the WENO subdomains enclosed with black bounding boxes. The remaining subdomains are accurately dealt with by the spectral method since all the essential small and large scale structures of the flow field are correctly represented in the hybrid solution. Once again, the number of WENO subdomains is far fewer than the spectral ones, resulting in a more efficient algorithm than the classical WENO scheme.

7. Conclusions

We have presented the one dimensional version of the multi-domain spatial and temporal adaptive Hybrid Spectral-WENO method for nonlinear systems of hyperbolic conservation laws. The main idea is to partition the physical domain into a grid of subdomains which are either a Chebyshev collocation grid for the spectral method or an uniformly spaced grid for the high order WENO method. High order multi-resolution analysis is used to measure the smoothness of the solution in a given subdomain in order to switch a subdomain from spectral to WENO when the solution becomes non-smooth, and vice versa. In this work, the Hybrid method was tested with the standard shock-tube test problems, the Shock-Entropy wave interaction and the Blastwave problems. The results matched the ones computed by the classical fifth-order WENO finite difference method. Timing results of preliminary two dimensional experiments, which are a much more meaningful measure of CPU costs than the one dimensional case, have shown a relevant speedup over the classical WENO scheme and can be found in more details at [1].

Currently, we are investigating the role of the multi-resolution tolerance parameter ϵ_{MR} and its effects on the Hybrid solution. Furthermore, the implementation of the smoothness measurements in the spectral subdomains can be improved and is under investigation. We plan to extend the Hybrid method to nonlinear hyperbolic conservation laws systems in higher dimensions with higher order WENO schemes.

Acknowledgements

The first author has been supported by CNPq, Grant 300315/98-8. The second author gratefully acknowledges the support of this work by the DOE under Contract No. DE-FG02-98ER25346 and the AFOSR under Contract No. FA9550-05-1-0123.

References

[1] B. Costa, W.S. Don, D. Gottlieb, R. Sendersky, Two-dimensional multi-domain hybrid spectral-WENO methods for conservation laws, Commun. Computat. Phys. 1 (2006) 548–574.

[2] W.S. Don, A. Solomonoff, Accuracy and speed in computing the Chebyshev collocation derivative, SIAM J. Sci. Comp. 16 (6) (1995) 1253–1268.
[5] D. Gottlieb, C.W. Shu, On the Gibbs phenomenon V: recovering exponential accuracy from collocation point values of a piecewise analytic function, Numer Mathemat 71 (1995) 511–526.
[6] D. Gottlieb, E. Tadmor, Recovering pointwise values of discontinuous data within Spectral accuracy, in: E. Murman et al., (Ed.), Progress and Supercomputing in Computational Fluid Dynamics, Proceedings of US–Israel Workshop, 1985, pp. 357–375 .
[7] A. Henrick, T. Aslam, J. Powers, Mapped weighted essentially non-oscillatory schemes: achieving optimal order near critical points, J. Comput. Phys. 207 (2005) 542–567.
[9] D.A. Kopriva, A multidomain spectral collocation computation of the sound generated by a shock-vortex interaction, in: D. Lee, M.H. Schultz (Eds.), Computational Acoustics: Algorithms and applications, vol. 2, Elsevier Science Publishers B.V., North Holland, IMACS, 1988.
[10] P.D. Lax, Accuracy and resolution in the computation of solutions of linear and nonlinear equations, in: Recent Advances in Numerical AnalysisProceedings of the Symposium on Mathematical Research Center, University of Wisconsin, Academic Press, 1978, pp. 107–117.
[12] E. Tadmor, Convergence of spectral methods for nonlinear conservation laws, SINUM 26 (1989) 30–44.
[13] Y. Maday, S.O. Kaber, E. Tadmor, Legendre pseudospectral viscosity method for nonlinear conservation laws, SIAM J. Numer. Anal. 30 (1993) 321–342.
[14] H. Vandeven, Family of spectral filters for discontinuous problems, J. Sci. Comp. 24 (1992) 37–49.
[15] W.S. Don, Numerical study of pseudospectral methods in shock wave applications, J. Comput. Phys. 110 (1994) 103–111.
[17] K. Sebastian, Multi domain WENO finite difference method with interpolation at sub-domain interfaces, J. Sci. Comput. 19 (2003) 405–438.
[18] P. Woodward, P. Collela, The numerical simulation of two dimensional fluid flow with strong shocks, J. Comput. Phys. 54 (1984) 115–173.
[23] A. Harten, High resolution schemes for hyperbolic conservation laws, Comput. Phys. 49 (1983) 357–393.
[24] A. Harten, Adaptive multiresolution schemes for shock computations, Comput. Phys. 115 (1994) 319–338.
[25] G.S. Jiang, C.W. Shu, Efficient implementation of weighted ENO schemes, J. Comput. Phys. 126 (1996) 202–228.
[28] M.S. Min, M.S. Kaber, W.S. Don, Fourier-Padé approximations and filtering for the spectral simulations of incompressible Boussinesq convection problem, Math. Comput., Publications du Laboratorie Jacques-Louis Lions, R03021, Math. Comput., in press.
[30] J.H. Jung, B.D. Shizgal, Generalization of the inverse polynomial reconstruction method in the resolution of the Gibbs phenomena, J. Comput. Appl. Math. 172 (1) (2004) 131–151.